

Article

A Polished-D-Shape SPR-Based Photonic Crystal Fiber Sensor with High Sensitivity for Measuring Refractive Index

Wangyoyo Li ¹, Menglin Jiang ², Jianjie Xu ³, Yu Chen ³ and Hui Zou ^{2,*}

¹ Bell Honors School, Nanjing University of Posts and Telecommunications, Nanjing 210023, China; b20040713@njupt.edu.cn

² College of Electronic and Optical Engineering & College of Flexible Electronics (Future Technology), Nanjing University of Posts and Telecommunications, Nanjing 210023, China

³ Portland Institute, Nanjing University of Posts and Telecommunications, Nanjing 210023, China

* Correspondence: huizou@njupt.edu.cn

Abstract: In the correspondence, a novel polished-D-shape photonic crystal fiber sensor structure on the basis of surface plasmon resonance is proposed for measuring analyte refractive index. With the help of the finite element method, sensing performances of the structure have been analyzed through numerical simulations along with a step-by-step optimization. In this design, different capillaries are gathered and processed to form a D-shape silica structure and nano-scale gold material is coated on the flattened surface. With utilization of a thin gold film and solid silica background, the resonance effect is excited and the loss curve has red shift along with an increase in refractive index, which is applied for sensing. From the simulation and calculation results, the final sensor structure achieves the optimal performance where values of maximum and average sensitivity reach 32,000 and 12,167 nm/RIU along with a sensing coverage of refractive index from 1.26 to 1.32. Also, the proposed design obtains a range of resonant wavelength from 1810 to 2540 nm. We believe the proposed sensor can be a potential candidate for organic and biological detection and related applications.

Keywords: photonic crystal fiber; surface plasmon resonance; refractive index sensor



Citation: Li, W.; Jiang, M.; Xu, J.; Chen, Y.; Zou, H. A Polished-D-Shape SPR-Based Photonic Crystal Fiber Sensor with High Sensitivity for Measuring Refractive Index. *Crystals* **2023**, *13*, 1282. <https://doi.org/10.3390/cryst13081282>

Academic Editor: Shih-Wen Chen

Received: 31 July 2023

Revised: 12 August 2023

Accepted: 17 August 2023

Published: 19 August 2023



Copyright: © 2023 by the authors. Licensee MDPI, Basel, Switzerland. This article is an open access article distributed under the terms and conditions of the Creative Commons Attribution (CC BY) license (<https://creativecommons.org/licenses/by/4.0/>).

1. Introduction

Surface plasmon resonance (SPR) is a kind of oscillation which gathers electrons from a conduction band and interacts with the periodical varying electric field generated from incident light [1]. In this optical effect, incident light is introduced with an appropriate incidence angle, which brings photons to the surface of plasmonic metal materials. These photons interact with surface-located electrons and further cause resonance where these original surface-located electrons appear to propagate parallel to the surface of plasmonic metal materials and create energetic plasmon electrons through non-radiation excitation [2,3]. When SPR occurs, a minuscule change in the refractive index (RI) in analyte or another medium in the environment in simple or complicated systems such as single-object or multi-physics can alter the phase-matching condition. Change of condition further influences the existence of the SPR effect [4,5]. This renders the measurement of analytes and related sensing technologies feasible for various systems, particularly in applications such as biomedical detection services in the face of global public health crises like the Coronavirus [6].

Photonic Crystals can be utilized as integrated optical devices which enhance interactions between light and matters [7]. Many applications have been demonstrated, such as all-optical logic gates [8], filters [9], highly efficient modulators [10], and sensors. For photonic-crystal-based sensors, there are two types. One type is based on an array of different number ring-slot and input–output line defect coupling waveguides, which places light sources vertically on the rods to connect waveguides from both input and output

paths [11]. This type has a small sensitivity value but has a narrow curve width on the nanometer scale. The second type is utilized in optical fibers. In recent decades, with a large quantity of research concentrating on photonic crystal fibers (PCFs) [12], it has been well concluded that PCFs can be effectively applied with the SPR effect for a reliable reason, as PCFs perfect optical properties along with different geometries and materials to choose for design [13,14]. A large amount of work has been carried out to design SPR-based PCF sensors to achieve good performances in the fields of measurement and detection. Some typical applications for single-object or multi-physics systems are known as liquid RI, salinity [15], temperature [16], magnetic field [17], etc.

There are a few types of SPR-based PCF sensors. The realization of the first type depends solely on various topological geometries and different plasmonic metal materials chosen for single-parameter measurement. In 2018, Chen et al. proposed a D-shaped SPR-based PCF applied as an RI sensor with numerical studies. Unlike normal D-shaped structures, this study employed an open-ring channel coated with a gold film to excite the SPR effect. Simulation results indicated that the sensor achieved a sensing range of RI from 1.20 to 1.29. When the analyte's RI exceeded 1.25, the anti-crossing effect started to appear and the peak value of the loss curve remained nearly constant with a change in RI. The proposed design achieved a maximum spectral sensitivity of 11,055 nm/RIU and a high resolution of about 9.05×10^{-6} RIU when RI was selected as 1.29 [18]. Some unusual shapes are also proposed. In 2023, Chao et al. proposed a novel trapezoidal-shaped temperature sensor. The fiber structure conducts two layers of elliptical air holes with different parameters and a polished trapezoidal-shape surface where thin silver and silica dioxide are deposited. Simulation results indicated that the sensor obtained a maximum temperature sensitivity and resolution up to 5200 pm/°C and 0.01923, respectively. Moreover, the temperature sensing range was from 10 to 60 °C [19].

The second type is focused on measurement in multi-channels to reach the scenario of multi-parameter sensing without considering cross influence. In 2020, Bing et al. proposed a dual-channel SPR-based PCF sensor that possessed the advantage of improving the detection efficiency of samples on different channels. In this design, a horizontal polished structure was proposed. The fiber structure was designed to be immersed directly in the liquid analyte to reduce coating difficulty and prevent microfluidic filling. Through the optimization of the dielectric layer, the ability to identify channels was efficiently improved. The wavelength sensitivities of two channels achieved 11,600 nm/RIU and 10,600 nm/RIU, respectively. The proposed structure was capable of simplifying the process complexity in multi-sample detection [20].

The third type focuses on a simultaneous performance in multi-physics systems for a multi-parameter sensing scenario. In 2019, Han et al. proposed a PCF structure with dual surface plasmon resonance to realize the measurement of temperature and strain while addressing the non-cross-sensitivity problem simultaneously. In this design, two holes in a symmetric relation of the fiber geometric were coated with gold coatings. One of those two holes was infiltrated with temperature-sensitive liquid in order to measure temperature. Simulation and calculation results indicate that the proposed design achieved simultaneous measurement of temperature and strain, with temperature sensitivities of -6.83 nm/°C and a strain sensitivity of 1.30 pm/ $\mu\epsilon$ with a scenario when diethylene glycol was chosen as the temperature-sensitive liquid [21].

In this article, an optimized novel SPR-based PCF sensor structure with a polished-D-shape is proposed for measurement of RI with high values of maximum and average sensitivity. Sensing performance of the fiber sensor structure has been analyzed through numerical simulations with approaches based on the finite element method (FEM). In the correspondence, different capillaries are gathered and processed to a polished-D-shape silica structure with nano-scale gold material coated on flattened surface. By applying a thin gold film and a solid silica-background core area to excite and enhance the SPR effect, the loss curve shifts towards longer wavelengths when the RI value increases. By optimizing structural parameters, the values of maximum and average sensitivity reach

32,000 and 12,167 nm/RIU, respectively, along with a sensing coverage of RI from 1.26 to 1.32, in steps of 0.01 RIU. Moreover, the resonant wavelength of the proposed design ranges from 1810 to 2540 nm.

Label-free sensors are systems that are capable of detecting physical, chemical and biological matter in micrometer and nanometer scales [22]. These devices have extraordinary sensitivity along with a fast time applied for measurement in numerous scenarios [23]. An SPR-based sensor is a kind of label-free sensor. Benefiting from these outstanding performances along with an intuitive geometrical structure, the proposed fiber sensor will have an advantage in the field of organic and biological detection and related applications.

This article is organized as follows: Section 1 is a brief introduction to the research background and the relationships between these abbreviations. Section 2 provides the geometry of proposed model and some parameters utilized in the study. Section 3 shows a comparison and corresponding analysis of related models concentrating on different sensing performances. Section 4 offers a detailed description of the effect of geometrical parameters on sensing performances. Section 5 conducts a simulation on the final optimized model and demonstrates a baseline comparison with similar studies. The summarized conclusions are presented in Section 6.

2. Model and Method of the Design

Figure 1a,b illustrate a 3D schematic and a 2D sketch of the proposed fiber sensor, respectively. Panel (i) demonstrates mode field distributions of the core region area A in x -polarization, which is utilized to measure RI.

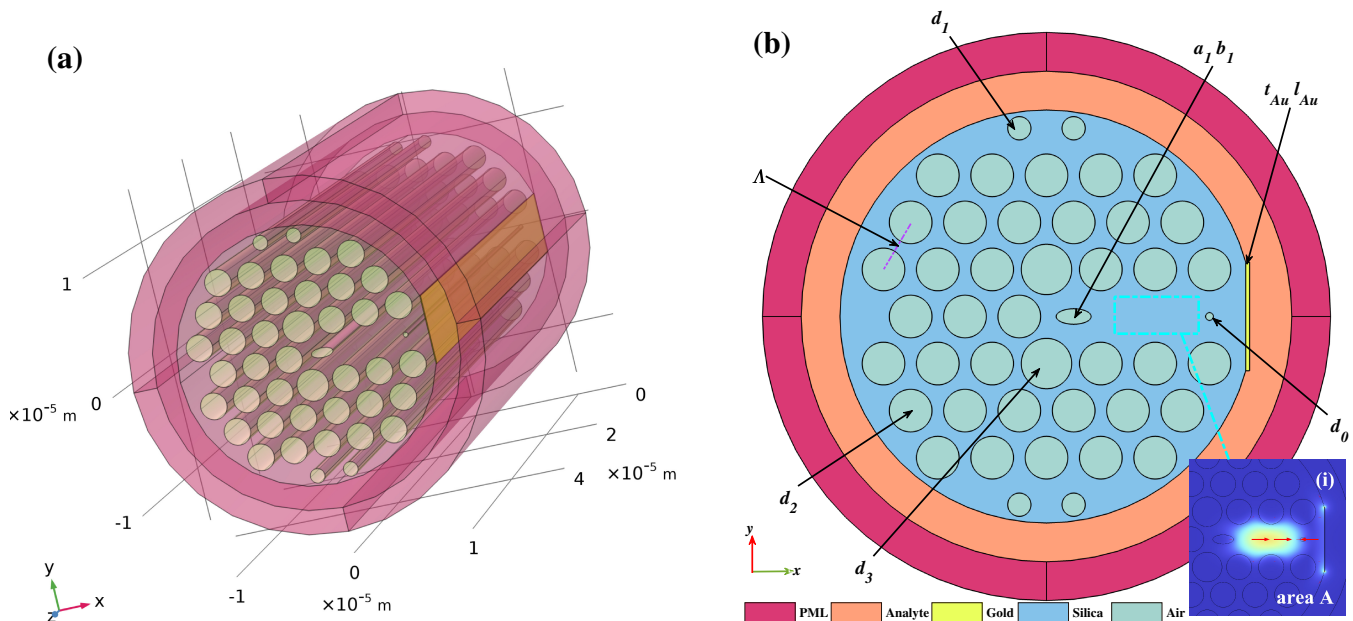


Figure 1. (a) A 3D schematic of the proposed fiber sensor. (b) A 2D sketch of the proposed fiber sensor. Panel (i) demonstrates mode field distributions of region area A in x -polarization.

The proposed cylinder structure is primarily composed of an area of an air hole array with a triangle lattice arrangement. The lattice spacing, which is interpreted as the distance between two nearby geometrical centers of the air holes in the array, is represented by Λ . In the initial design, the structure was simplified, with all air holes having same radius as d_2 . To excite the SPR effect, part of the silica structure is polished to form a flattened plain and nano-scale gold material is coated on the surface. The thickness and width of the coating are presented by t_{Au} and l_{Au} . For convenience, these two parameters are abbreviated as t and L .

In further improvement, six air holes at the tips of the array are removed and four air holes at the edge of the upper and lower array are narrowed to a smaller radius denoted by d_1 , which aims to decrease the silica-background area between the air hole array and external part in order to concentrate more energy on the solid-silica-background core area and further improve sensing performances. The solid-silica-background core area is named core area A, which generates the core mode. Area A is formed by removing two air holes, which is illustrated in the sky-blue rectangular area in Figure 1b.

In related works, it has been found that elliptical holes demonstrates a superior performance to circular holes as they are capable of remarkably affecting the coupling energy between the core mode and the surface plasmon polariton mode (SPP) [24]. Thus, the air hole on the left side of area A is replaced with a horizontally placed elliptical hole with semi-major and semi-minor axes, denoted by a_1 and b_1 . For convenience, these two parameters are abbreviated as a and b . A tiny air hole with a radius denoted by d_0 is added on the right side of area A in order to further strengthen the SPR effect. The adjacent two air holes of the elliptical hole are magnified to a larger radius denoted as d_3 in order to extrude the core region and to make sure most of the energy from area A interacts with the thin gold film on the right side, thereby improving sensing performances. On the external side of the silica structure, liquid analyte is introduced.

Figure 2a illustrates the 2D schematic of the proposed fiber sensor in the process of fabrication. For the proposed structure, it can be practically realized with the well-known stack-and-draw fabrication technique [25]. In manufacturing procedures, an external container is applied to gather a variety of different rods and capillaries at the start-up stage. In the correspondence, thick-wall, thin-wall, elliptical-core and square circular-core fiber capillaries are utilized as basic units to form initial holes, large holes, elliptical core and tiny air hole, respectively. Some simple auxiliary solid rods and two little-bit-complicated auxiliary polished solid rods are applied as the removed air holes in order to fix the position inside the container and create core region area A during the assembly process. An elliptical-core capillary is used to create the elliptical hole on the left side of area A. In addition, a special circular-core square capillary is embedded in these two auxiliary polished solid rods in order to form the tiny air hole and fix its position in the fabrication process. After gathering these rods and capillaries together in a symmetry-shaped hexagonal external container, liquid silica is infiltrated into the space among these micro structures. At this moment, the start-up hexagonal structure is made. The structure is then embedded into a hollow cylinder external container and filled with liquid silica once again to form a cylinder-shaped fiber structure. Then, the structure is shaped into a polished D-shape fiber, and plasmonic metal material, namely nano-scale gold, is coated onto the flattened surface. Subsequently, the final structure of the proposed design is fully realized.

Figure 2b demonstrates a cross-sectional FEM mesh of the proposed fiber sensor in simulations. In the correspondence, the finite element method is used for solving eigenmode with a quantity of square and triangle grids in numerical simulations. Furthermore, a perfectly matched layer (PML) is designed at the exterior part of the analyte area to cut off regions beyond the analyte area and limit the computational area for numerical simulation by absorbing all radiation energy at the edge of the PML region. The thickness of PML is designed as $t_{PML} = 2.0 \mu\text{m}$. The numerical studies and results are simulated and calculated with the help of Wave Optics Module in the software COMSOL Multiphysics 6.0.

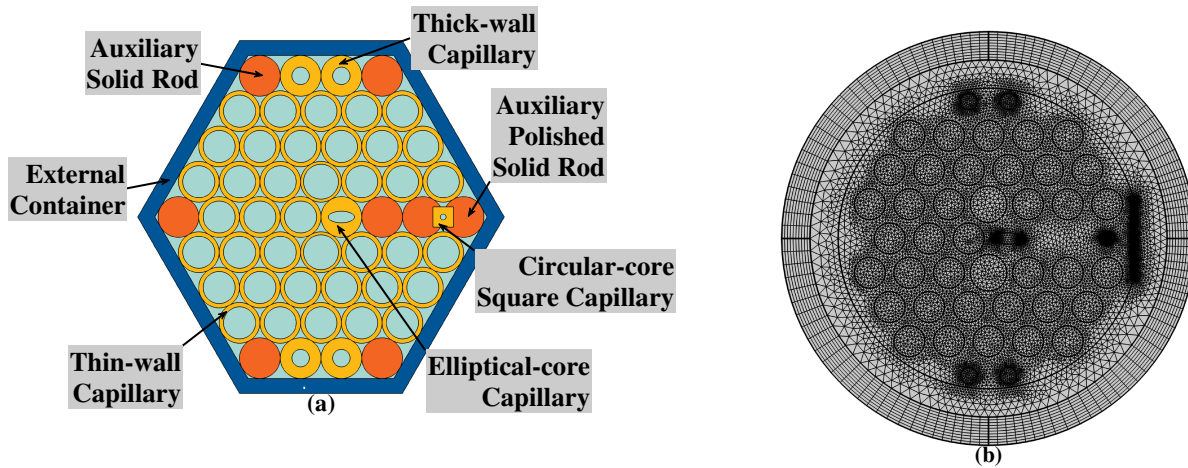


Figure 2. (a) A 2D schematic of the proposed fiber sensor in the process of fabrication. (b) A cross-sectional FEM mesh of the proposed fiber sensor in simulations.

Fused silica is chosen for its superior properties and physical performances. It is designed as the background base material of the sensor structure. The material refractive index of fused silica is obtained by a third-order Sellmeier Equation (1),

$$n_{Silica}^2 = 1 + \frac{A_1\lambda^2}{\lambda^2 - B_1^2} + \frac{A_2\lambda^2}{\lambda^2 - B_2^2} + \frac{A_3\lambda^2}{\lambda^2 - B_3^2} \quad (1)$$

where λ is the wavelength in free-space, measured in nanometers. The value of coefficients $A_i, B_i (i = 1, 2, 3)$ are given in Table 1 in a non-dimensional form. These coefficients are suitable for the wavelength range in this work [26,27].

Table 1. Coefficients of the third-order Sellmeier Equation.

Numerator Denotations	Values	Denominator Denotations	Values
A_1	0.6961663	B_1	0.0684043
A_2	0.4079426	B_2	0.1162414
A_3	0.897479	B_3	9.896161

Nano-scale gold is a kind of plasmonic metal material. It is coated at the polished surface near the core region to excite the SPR effect. The dispersion of nano-scale gold is obtained through the Lorentz–Drude model expressed by Equation (2) [28,29].

$$\epsilon_m = \epsilon_\infty - \frac{\omega_D^2}{\omega(\omega - j\gamma_D)} - \frac{\Delta\epsilon \cdot \Omega_L^2}{(\omega^2 - \Omega_L^2) - j\Gamma_L\omega} \quad (2)$$

where $\epsilon_\infty = 5.9673$ stands for the dielectric constant in a scenario where frequency is ultra-high, and $\omega = 2\pi c/\lambda$ is the angular frequency of the light propagating through the PCF system. $\Delta\epsilon = 1.09$ is the weight factor. ω_D and γ_D represent the plasma and damping frequency, respectively. Ω_L and Γ_L are the frequency and spectral width of the Lorentz oscillator, respectively. Ω_L and Γ_L are $2\pi \times 650.07 \times 10^{12}$ rad/s and $2\pi \times 104.86 \times 10^{12}$ rad/s in angular frequency.

It is widely known that PCFs have multiple types, including high-birefringence (Hi-Bi) PCFs and SPR-based PCFs. Most Hi-Bi PCFs have cladding layers without plasmonic metal materials. This type has high index contrast and can be applied as polarization-maintaining fibers, which are capable of eliminating the effect of polarization mode dispersion or of stabilizing the operation of optical devices [30]. SPR-based PCFs are coated with plasmonic metal materials. It works on the basis of interactions between electrons on the surface of

the plasmonic metal materials along with the evanescent field [31,32]. In SPR-PCF sensor systems, when light with an appropriate incident angle propagates through the structure, some part of the light penetrates through the air hole array and undergoes interactions with plasmonic metal materials coated on the polished surface. The interactions generate free electrons excited from surface. SPR-PCF sensor systems use different-order SPP modes and core modes to produce the SPR effect [33]. When the evanescent field of the incident light reaches a frequency that matches with the frequency of free electrons generated from the surface of plasmonic metal materials, the resonance effect is thus fully generated along with the surface plasmon wave [34]. This phenomenon is characterized by confinement loss (CL), which is a good metric to represent the loss when the light propagates through the system. The CL value is obtained by calculation calculation Equation (3) [35],

$$CL = 8.686 \times \frac{2\pi}{\lambda} \times \text{Im}(n_{eff}) \times 10^4 \quad (3)$$

where n_{eff} represents the effective RI of the coupled mode. The value of CL is measured in dB/cm. When the phase-matching condition is achieved, a loss peak occurs in the loss curve. The resonance peak will witness a red or blue shift with a change in the RI value of the dielectric medium, such as a sample or analyte. which is adjacent to the surface. The change of peak value reflects the concentration of the medium [36].

Figure 3a demonstrates the CL curve of the coupled mode in both x - and y -polarization along with the real part of the effective RI of the coupled mode in both the core mode and the SPP mode with RI selected as 1.28 with a list of geometrical parameters in the proposed structure in the initial stage: $a = 0.9 \mu\text{m}$, $b = 0.4 \mu\text{m}$, $d_0 = 0.2 \mu\text{m}$, $d_1 = 0.6 \mu\text{m}$, $d_2 = 1.1 \mu\text{m}$, $d_3 = 1.3 \mu\text{m}$, $t = 60 \text{ nm}$, $l = 5.6 \mu\text{m}$, $\Lambda = 2.8 \mu\text{m}$. Furthermore, Figure 3b–d illustrate the mode field distributions of the coupled mode in x -polarization when the wavelength is selected as 1760, 1920, and 2300 nm, respectively. From Figure 3a, the core mode in area A is completely coupled with the SPP mode on the surface of the polished nano-scale Au-coated plane when the wavelength is selected as 1920 nm. In some parts of the wavelength regions, the value of confinement loss is close to zero. Thus, it can be approximated that resonance almost does not exist. A reasonable explanation for this phenomenon is considered to be that in those wavelength regions, most of the energy is bound in the core region, as depicted in Figure 3b and d. When it reaches an appropriate resonant wavelength denoted by λ_{SPR} , the SPR effect is fully excited, with the core mode completely coupled with the SPP mode. During this time, the mode field distribution and energy distribution transition from the core area to the polished surface of the nano-scale Au coating, accumulating the largest amount of energy in a small space with a high energy density, as illustrated in Figure 3c. This density reaches 160, which is higher than the values of 90 and 100 in Figure 3b and d, respectively. At this point, the phase-matching condition is fully achieved, observed at the intersection between the yellow solid curve and the green solid curve in Figure 3a. At this intersection, the CL curve peaks. Furthermore, Figure 3a shows that modes coupled in different polarization states exhibit a significant difference. In the x -polarization, the curve has a large value in terms of dB/cm-scale. In the y -polarization, the CL value is close to zero. This further indicates that the proposed design achieves well-performing single-polarization sensing. In the subsequent parts of this work, we will select x -polarization for research and analysis.

The variation in RI has an influence on the effective RI of the coupled mode in the SPR-excited region in the x -polarization. This, in turn, alters the mode field distributions in the area. The corresponding value of the resonance wavelength also changes. Eventually, the CL curve will exhibit either a red-shift or a blue-shift, depending on the variation in the peak value of these curves. Therefore, it is significant to seek evaluation schemes to measure the combined impact of the varying structural parameters on the affected sensing performances. Under this scenario, it is appropriate to characterize the relationship between

changes in the *CL* curves and variations in RI. Therefore, the RI sensitivity, denoted as S_n , can be a good metric, and it is obtained through the following equation [37],

$$S_n = \Delta\lambda_{SPR} / \Delta n_a \tag{4}$$

where $\Delta\lambda_{SPR}$ is the change of resonant wavelength value and Δn_a denotes the varying RI with a step of 0.01 RIU. The unit of S_n is nm/RIU.

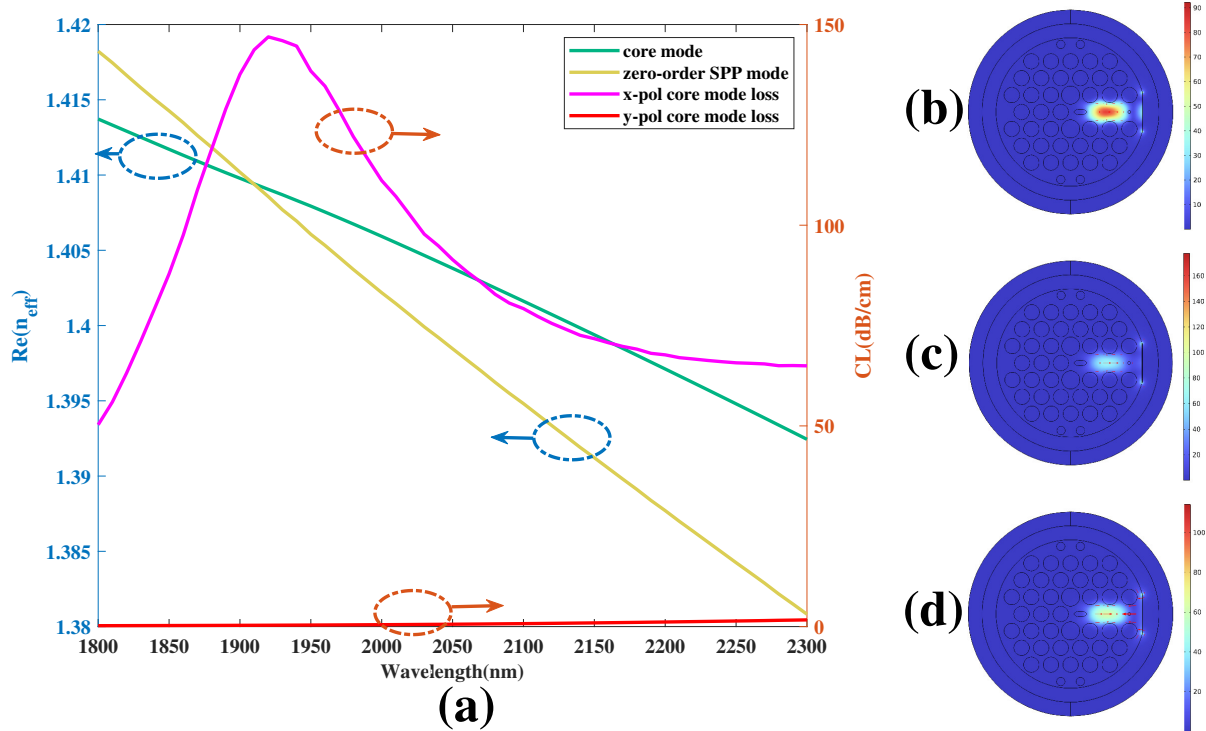


Figure 3. (a) *CL* curve of coupled mode in both *x*- and *y*-polarization along with the real part of effective RI of coupled mode from core modes and SPP mode with RI selected as 1.28. (b–d) The mode field distributions of coupled mode in *x*-polarization when wavelength is selected as 1760, 1920, and 2300 nm, respectively.

Also, amplitude sensitivity, which is denoted as S_a or *AS*, is introduced as a another useful metric. It can reflect the relationship between the curve intensity of the *CL* spectra along with the variation sequence of RI. It is defined as Equation (5), the equation below,

$$S_a = -(\Delta CL / \Delta n_a) / CL_{initial} \tag{5}$$

where ΔCL is the change of confinement loss value and $CL_{initial}$ denotes the initial confinement loss. Metric S_a has a unit of RIU^{-1} .

In addition, another important metric can combine sensitivity performances along with the shape of the *CL* curve in the proposed sensor. This is the figure of merit, which is denoted as *FOM*. This metric focuses on the full width at half of the maximum (FWHM) value. The calculation of this metric is presented by Equation (6),

$$FOM = S_n / FWHM \tag{6}$$

where the unit of *FWHM* is nanometers.

Figure 4 presents a possible implementation of the experimental setup of the SPR sensor for detecting analyte RI. Initially, a broadband light source is employed to direct initial light through a polarizer. In this work, the light exits the polarizer as *x*-polarized light. Subsequently, the light passes through the light controller device and enters a single-mode

fiber (SMF). The SMF is capable of receiving light and transitioning it into an environment suitable for PCF. Molecules in the liquid analyte are utilized for measurement and sensing. These molecules pass through a mass flow controller, serving as the inlet to enter the sensor, and then as the outlet to flow out of the sensor. These interactions lead to the SPR effect and cause a red or blue shift in the loss curve, which can be observed using an optical spectrum analyzer (OSA). The relevant data can be visualized via a computer [38].

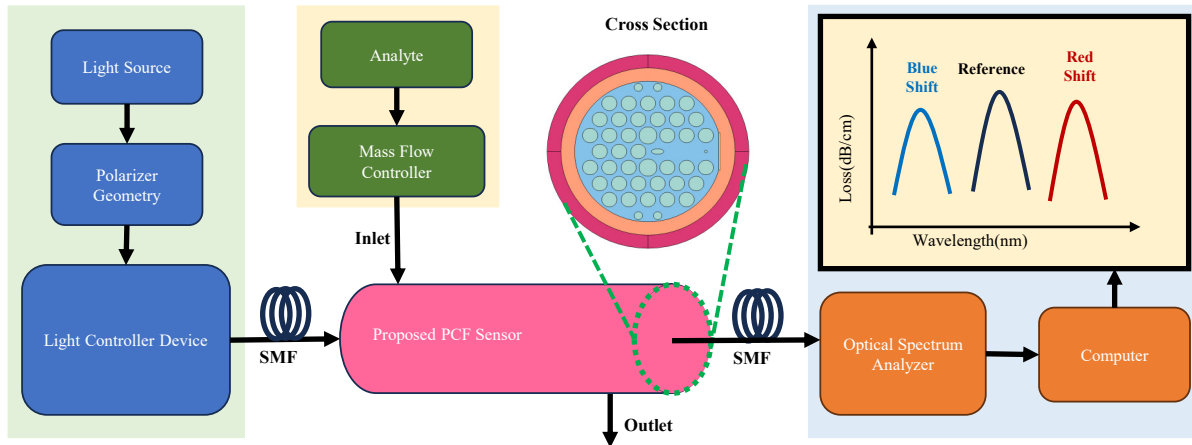


Figure 4. Possible implementation of the experimental setup of SPR sensor for detecting analyte RI.

3. Geometrical Comparisons

In this section, a variety of related geometrical designs are compared and analyzed.

Figure 5 shows the comparison of four 2D schematics of the design. In Figure 5a, a symmetrical construction design is applied to form a dual-core sensor structure with an elliptical core set at the central location to isolate these two core areas. Figure 5b is the initial design. In Figure 5c, a small air hole is added on the left side of the air hole array to concentrate the mode field distribution on core region area A. In Figure 5d, two circular air holes are replaced with elliptical air holes pointing to the core area in order to alter the region for the SPR effect and change the sensing performance.

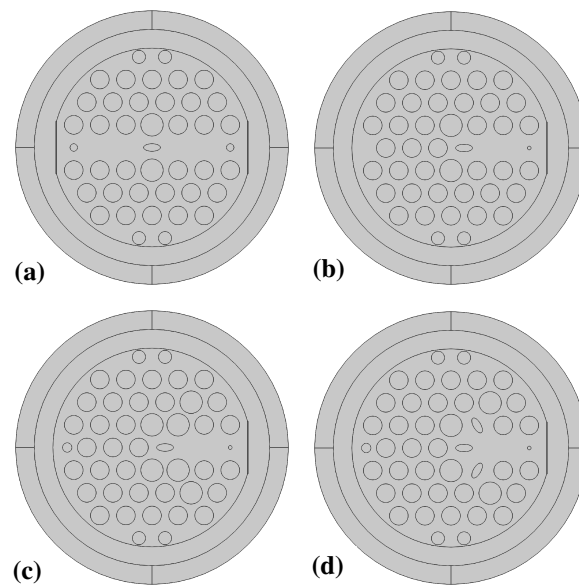


Figure 5. Comparison of four 2D schematics of the design. (a) A symmetrical dual-core structure. (b) The proposed structure. (c) Left-side hole added based on proposed design. (d) A structure with more elliptical holes.

Figure 6 demonstrates CL curves of the coupled mode in x -polarization of four compared structures with different ranges of analyte RI.

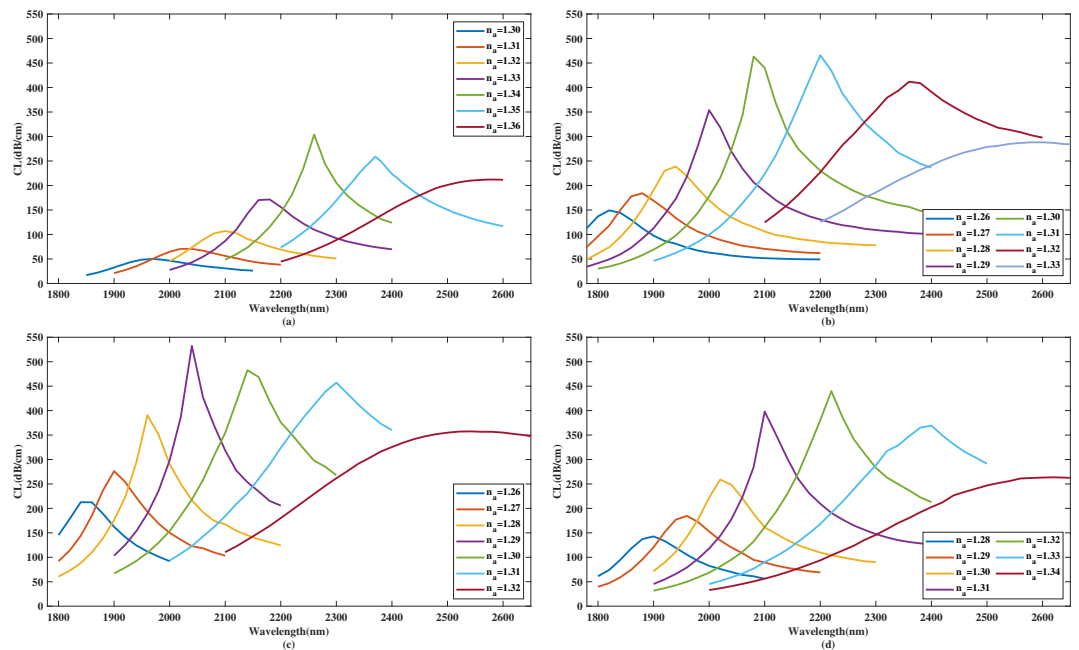


Figure 6. CL curves of coupled mode in x -polarization of four compared structures with different range of analyte RI.

In Figure 6a, with an increase in the sequence of RI with a changing range from 1.30 to 1.36, the CL curve of the coupled mode in the core area in x -polarization undergoes a long-distance red-shift. Additionally, the corresponding peak value of the CL curve shows a trend from increase to decline. With the red shift, λ_{SPR} follows a changing sequence: 1970, 2025, 2100, 2175, 2260, 2370, 2580 nm, with RI respectively selected as 1.30, 1.31, 1.32, 1.33, 1.34, 1.35, 1.36. According to calculation using Equation (4), the corresponding S_n values are obtained as 5500, 7500, 7500, 8500, 11,000, and 21,000 nm/RIU, respectively. The sensing range of RI in this scenario is from 1.30 to 1.36. Additionally, the average value of S_n is calculated as 10,167 nm/RIU.

In Figure 6b, with an increase in the of RI with a changing range from 1.26 to 1.33, the CL curve of the coupled mode of the core area in x -polarization undergoes a significant red-shift. In addition, the corresponding peak value of the CL curve demonstrates a trend from increase to decrease. With the red shift, λ_{SPR} has a changing sequence: 1820, 1880, 1940, 2010, 2090, 2220, 2360, 2600 nm with RI set as 1.26, 1.27, 1.28, 1.29, 1.30, 1.31, 1.32, 1.33, respectively. According to Equation (4), the corresponding S_n values are obtained as 6000, 6000, 7000, 8000, 11,000, 14,000 and 24,000 nm/RIU, respectively. The sensing range of RI in this model is from 1.26 to 1.33. In addition, the average value of S_n is calculated as 11,000 nm/RIU.

In Figure 6c, with an increase in the sequence of RI within a changing range from 1.26 to 1.32, the CL curve of the coupled mode in the core area in x -polarization witnesses a significant red-shift. Additionally, the corresponding peak value of the CL curve shows a trend from rise to decrease. With the red shift, λ_{SPR} follows a changing sequence: 1850, 1900, 1970, 2050, 2150, 2300, 2540 nm, when RI is 1.26, 1.27, 1.28, 1.29, 1.30, 1.31, 1.32, respectively. According to calculations using Equation (4), the corresponding S_n values are obtained as 5000, 7000, 8000, 10,000, 15,000, and 24,000 nm/RIU, respectively. The sensing range of RI in this scenario ranges from 1.26 to 1.32. Additionally, the average value of S_n is calculated as 11,600 nm/RIU.

In Figure 6d, with an increase in the sequence of RI within a changing range from 1.28 to 1.34, the CL curve of the coupled mode in the core area in x -polarization witnesses a

significant red-shift. Additionally, the corresponding peak value of the CL curve shows a trend from increase to decline. With the red shift, λ_{SPR} follows a changing sequence: 1900, 1960, 2020, 2100, 2220, 2400, 2620 nm, with RI respectively chosen as 1.28, 1.29, 1.30, 1.31, 1.32, 1.33, 1.34. According to calculations using Equation (4), the corresponding S_n values are obtained as 6000, 6000, 8000, 12,000, 18,000, and 22,000 nm/RIU, respectively. The sensing range of RI in this scenario ranges from 1.28 to 1.34. Additionally, the average value of S_n is calculated as 12,000 nm/RIU.

Figure 7 shows AS curves of coupled mode in x -polarization of four compared structures with different range of analyte RI.

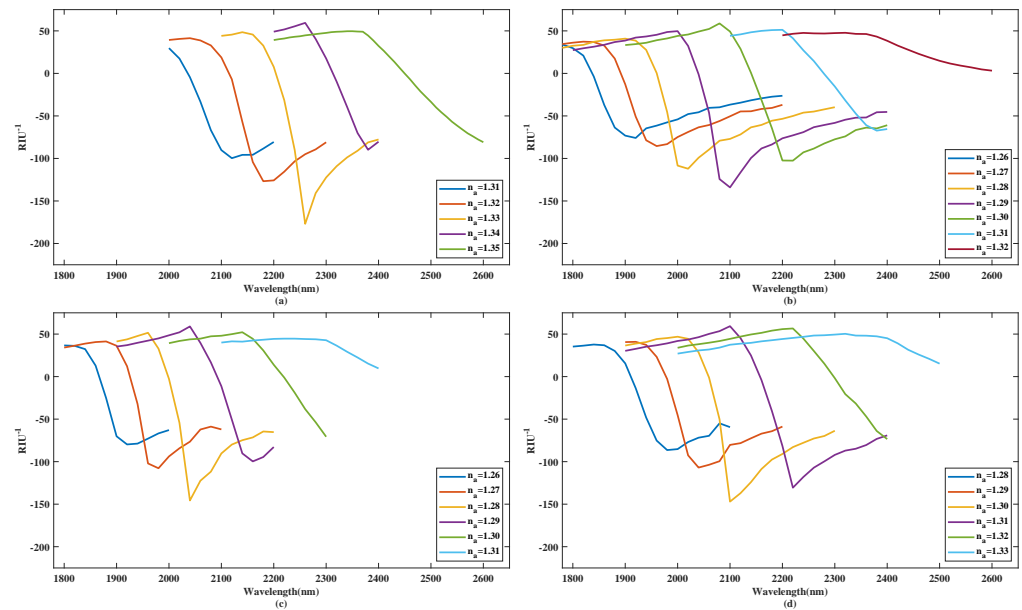


Figure 7. AS curves of coupled mode in x -polarization of four compared structures with different range of analyte RI.

In Figure 7a, with an increase in the sequence of RI within a variation range from 1.31 to 1.35, the AS curve of the coupled mode in the core area in x -polarization witnesses a long-distance red-shift. The λ_{peak} value, which represents the corresponding wavelength of the peak of the AS curve in the negative semi-axis, follows a changing sequence: 2120, 2180, 2030, 2260, 2380, 2600 nm, when RI is 1.31, 1.32, 1.33, 1.32, 1.35, respectively. According to calculations using Equation (5), the corresponding absolute values of S_n are obtained as 99.69, 126.8, 176.9, 89.79, and 80.88 RIU^{-1} , respectively.

In Figure 7b, with an increase in the sequence of RI within a variation range from 1.26 to 1.32, the AS curve of the coupled mode in the core area in x -polarization witnesses a dramatically red-shift. The λ_{peak} value follows a changing sequence: 1920, 1960, 2020, 2100, 2220, 2380, 2600 nm, with RI respectively set as 1.26, 1.27, 1.28, 1.29, 1.30, 1.31, 1.32. According to calculations using Equation (5), the corresponding absolute values of S_n are obtained as 75.92, 85.46, 112.1, 134.1, 102.6, 67.27, and 3.213 RIU^{-1} , respectively.

In Figure 7c, with an increase in the sequence of RI within a variation range from 1.26 to 1.31, the AS curve of the coupled mode in the core area in x -polarization witnesses a drastically red-shift. The λ_{peak} value shows a changing sequence: 1920, 1980, 2040, 2160, 2300, 2400 nm, with RI respectively selected as 1.26, 1.27, 1.28, 1.29, 1.30, 1.31. According to calculations using Equation (5), the corresponding absolute values of S_n are obtained as 79.75, 107.8, 145.6, 99.71, 70.7, and 9.624 RIU^{-1} , respectively.

In Figure 7d, with an increase in the sequence of RI within a variation range from 1.28 to 1.33, the AS curve of the coupled mode in the core area in x -polarization witnesses a significant red-shift. The λ_{peak} value has a changing sequence: 1980, 2040, 2100, 2220, 2400, 2500 nm, with RI respectively chosen as 1.28, 1.29, 1.30, 1.31, 1.32, 1.33. According to

calculations using Equation (5), the corresponding absolute values of S_a are obtained as 86.39, 107, 147, 130.6, 73.49, and 15.25 RIU^{-1} , respectively.

For the model illustrated in Figure 5a, this design is a dual-core type of SPR-PCF sensor, which is significantly different from the other three single-core sensing models. As a result, it exhibits different loss curve distributions, including curve width and curve intensity, as well as the sensing range for refractive index (RI). In the models shown in Figure 5b and c, the most notable disparity lies in the existence of a small air hole on the left side. Thus, the loss curve distribution is almost the same, with the exception of an additional RI sensing range of 1.33, along with numerically different sensing performances.

For the models illustrated in Figure 5c,d, the most significant difference is the variation in the core area geometry, specifically the number of elliptical air holes used. Consequently, the loss curve distributions for these two models exhibit visible differences, particularly in terms of the sensing range of RI and curve width. Taking into consideration both the fabrication feasibility and the pursuit of improved performance, including RI sensing range and sensitivities, the schematic in Figure 5b is chosen as the final proposed geometrical structure for analysis and optimization.

4. Simulation Results and Formal Analysis

Figure 8 illustrates the CL curve of the coupled mode in x -polarization when Λ is chosen as 2.6, 2.8, 3.0 μm , and RI is changing from 1.26 to 1.33 with a step of 0.01 RIU.

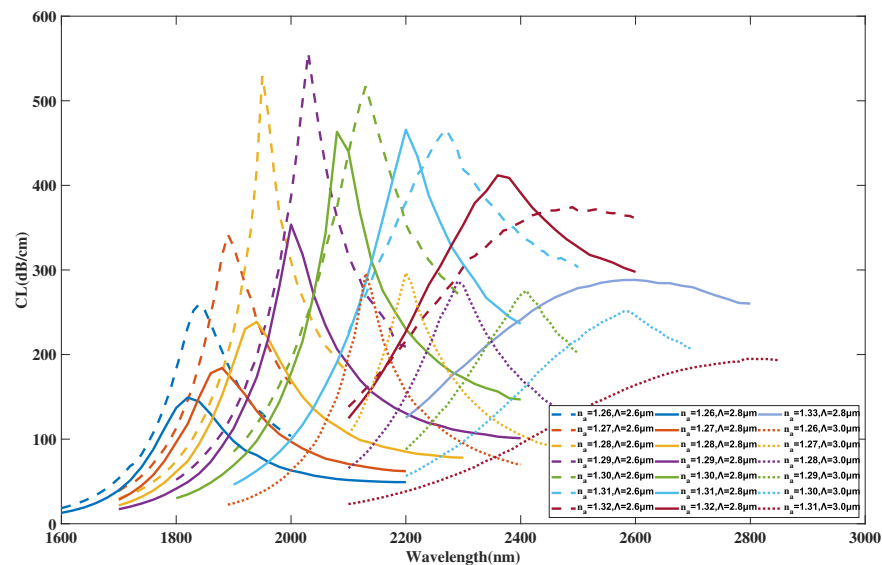


Figure 8. The CL curve of coupled mode in x -polarization when Λ is chosen as 2.6, 2.8, 3.0 μm , and RI is changing from 1.26 to 1.33 with a step of 0.01 RIU.

From Figure 8, as the value of Λ rises from 2.6 to 3.0 μm , the CL spectra begin to red-shift along with a decrease in curve intensity. The sensing coverage of RI widens to 1.33 when Λ is set at 2.8 μm , and it narrows to 1.31 when Λ is chosen as 3.0 μm . Moreover, with the increase in the value of Λ , the envelope of CL curves corresponding to varying RI shifts to the red and the curve intensity decreases.

The reason for these changes is considered to be that as the value of Λ increases, the core area A expands, and the arrangement of the air hole array becomes looser. This alteration affects the mode field distributions of the coupled mode in x -polarization within area A . Consequently, it modifies the phase-matching condition and the range of RI sensing, resulting in the emergence of new detected RIs such as 1.32 and 1.33 when Λ increases. Additionally, with the increase in the value of Λ , the expanding core area leads to a portion of the energy not being effectively concentrated in the area. As a result, the intensity of the envelope visibly decreases.

According to calculation using Equation (4), the maximum values of S_n are achieved as 22,000, 24,000, and 22,000 nm/RIU when Λ is respectively set to 2.6, 2.8, and 3.0 μm . The calculated results clearly indicate that the maximum value of S_n in the proposed design exhibits a trend of rise followed by a decline as Λ increases from 2.6 to 3.0 μm , with a peak value attained at Λ of 2.8 μm . Furthermore, the average S_n values achieved are 10,713, 11,000, and 13,400 nm/RIU with Λ set to 2.6, 2.8, and 3.0 μm , respectively. Taking into consideration both the maximum S_n values and the coverage of measurable RIs, it is evident that the proposed sensor structure achieves the best sensing performance when Λ is set to 2.8 μm .

Figure 9 demonstrates the CL curve of the coupled mode in x -polarization when d_2 is selected as 1.0, 1.1, 1.2 μm , and RI is selected as 1.26, 1.31, 1.32 and 1.33.

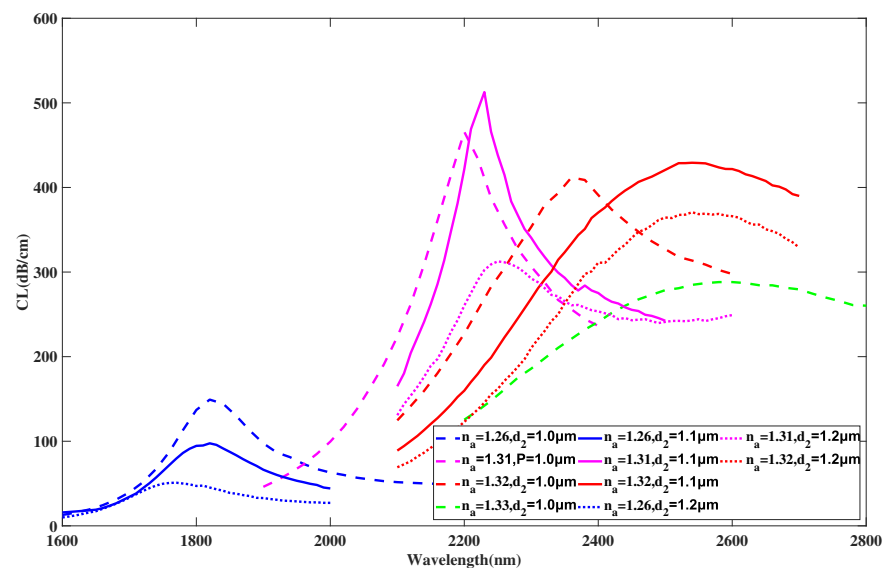


Figure 9. The CL curve of coupled mode in x -polarization when d_2 is selected as 1.0, 1.1, 1.2 μm , and RI is selected as 1.26, 1.31, 1.32 and 1.33.

From Figure 9, as the value of d_2 rises from 1.0 to 1.2 μm , the CL curve of the coupled mode in x -polarization starts to blue-shift and the curve intensity has a noticeable fall when RI is set as 1.26. The CL curve of the x -polarized mode with RI set to 1.31 and 1.32 has a noticeable red-shift and the intensity of spectra shows a trend from rise to decline. Sensing coverage of RI is extended to 1.33 when d_2 is set to 1.0 μm . In addition, when d_2 increases, the envelope of CL curves associated with varying RI appears to shift to the red along with the occurrence of a trend from increase to decrease in envelope intensity. The reasons for these changes are considered to be that when the value of d_2 becomes larger, core area A is gradually compressed, which concentrates the energy. However, the channel between the core area and the coating surface narrows due to the increasing d_2 value, making the arrangement of the air hole array compact, which causes the intensity of the envelope to trend from ascending to descending. Also, the change of mode field distributions influences the phase-matching condition of the x -polarized coupled mode on a very small scale, which further causes the sensing scope to be extended to 1.33 when d_2 is chosen as 1.0 μm . According to calculation in Equation (4), maximum values of S_n are achieved as 24,000, 31,000, 29,000 nm/RIU when d_2 is set as 1.0, 1.1, 1.2 μm , respectively. It is obvious from the calculation results that the maximum value of S_n in the proposed design has a trend from rise to decrease when d_2 has an increase sequence from 1.0 to 1.2 μm and achieves a peak value with d_2 selected as 1.1 μm . Moreover, the average S_n values achieved are 11,000, 12,000, 12,833 nm/RIU when d_2 is selected as 1.0, 1.1, 1.2 μm , respectively. When the maximum S_n value is given priority to be taken into consideration,

the value of d_2 is finally set as 1.1 μm when the proposed sensor structure gains an optimal sensing performance.

Figure 10 shows the CL curve of the coupled mode in x -polarization when d_3 is set as 1.1, 1.2, 1.3 μm , and RI is selected as 1.26, 1.31, 1.32.

From Figure 10, with a rising value of d_3 from 1.0 to 1.2 μm , the CL curves of the coupled mode in x -polarization with all chosen RI values almost stay still. The curve intensity when RI is chosen as 1.26 has a subtle increase and a shift of the curve does not occur. The curve intensity with RI selected as 1.32 first increases and then decreases. In addition, with the increase of d_3 , the envelope of CL curves associated with varying RI becomes narrow and curve intensity shows a decrease with minor changes. The reasons for these changes are considered to be that when the value of d_3 becomes larger, the core area A in x -polarization is compressed to a certain degree, ensuring more energy interaction with the right-side plasmonic metal material. However, the change of the d_3 value has a small effect due to the limited range of variation in the fabrication process. Also, there is a long distance from d_3 -radius air holes to the core area, which causes the CL curve and peak to show a small change. Moreover, the change of the mode field distribution of x -polarized area A influences the phase-matching condition and causes the CL curve and peak to shift slightly. According to calculation in Equation (4), the maximum values of S_n are achieved as 31,200, 31,000, 31,500 nm/RIU when d_3 is selected as 1.1, 1.2, 1.3 μm . It is obvious from the calculation results that the maximum value of S_n in the proposed design shows a trend from climbing to falling when d_3 has a varying sequence from 1.1 to 1.3 μm . Moreover, the calculated average value of S_n in the proposed design rises when d_3 has a changing sequence from 1.1 to 1.3 μm and achieves an ideal large value when d_3 is selected as 1.3 μm . Additionally, the average S_n values achieved are 11,916, 12,000, 12,000 nm/RIU when d_3 is selected as 1.1, 1.2, 1.3 μm , respectively. To make sure most of the energy can interact with the right side of the thin gold film with high sensitivity values, the d_3 is finally set to 1.3 μm when the proposed sensor structure achieves an optimal sensing performance.

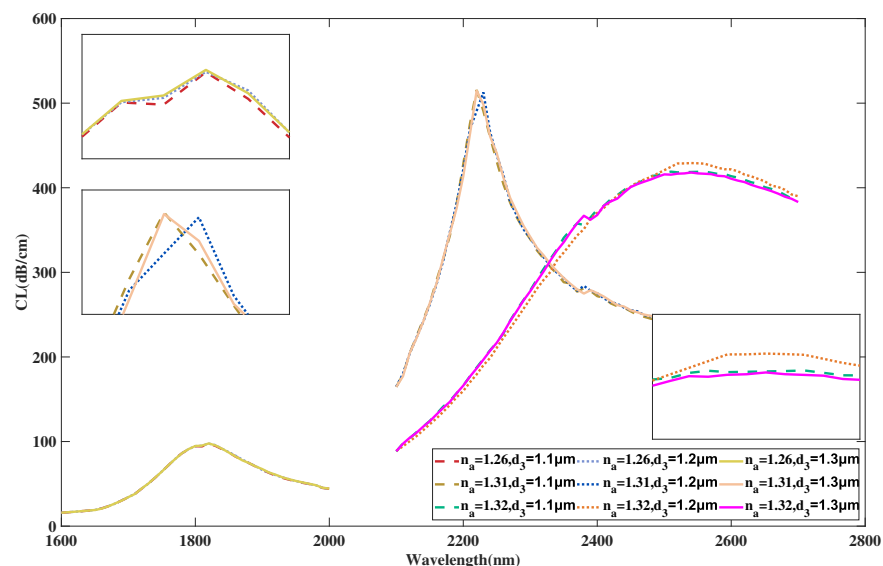


Figure 10. The CL curve of coupled mode in x -polarization when d_3 is set as 1.1, 1.2, 1.3 μm , and RI is selected as 1.26, 1.31, 1.32.

Figure 11 illustrates the CL curve of the coupled mode in x -polarization when d_1 is selected as 0.6, 0.7, 0.8 μm , and RI is chosen as 1.26, 1.31, 1.32. From Figure 11, with a rising value of d_1 from 0.6 to 0.8 μm , the CL curves with all chosen RI values almost stay still. The intensity of the CL curve when RI is selected as 1.26 has a subtle decrease. The curve intensity when RI is selected as 1.32 first increases and then decreases. In addition, with d_1

increasing, the envelope of CL curves associated with varying RI become wider and the curve intensity decreases with minor changes. Reasonable explanations for these changes are considered to be that when the value of d_1 becomes larger, core area A does not change, but the mode field distributions are altered by the solid-silica area between the air hole array and the exterior analyte. However, variation of d_1 values has little effect due to the limited range of variation in fabrication along with the far distance between d_1 -radius air holes and the core area, which causes a very small shift of the CL peak and curve. Moreover, the changes have little effect on the phase-matching condition of the x -polarized coupled mode of area A and further causes the CL curve and peak to show a slight shift. According to calculation in Equation (4), the maximum values of S_n are achieved as 32,200, 31,500, 30,000 nm/RIU when d_1 is selected as 0.6, 0.7, 0.8 μm , respectively. It is obvious from the calculation results that the maximum S_n value of the proposed structure gradually drops when d_1 has a variation sequence from 0.6 to 0.8 μm . Moreover, the average S_n values achieved are 12,000, 12,000, 11,067 nm/RIU when d_1 is selected as 0.6, 0.7, 0.8 μm , respectively. In this work, efforts are made to ensure most of the energy is concentrated in core area in order to further improve performances. Taking these issues, especially sensing sensitivities, into consideration, the value of d_1 is finally set as 0.6 μm when the proposed sensor structure reaches an optimal sensing performance.

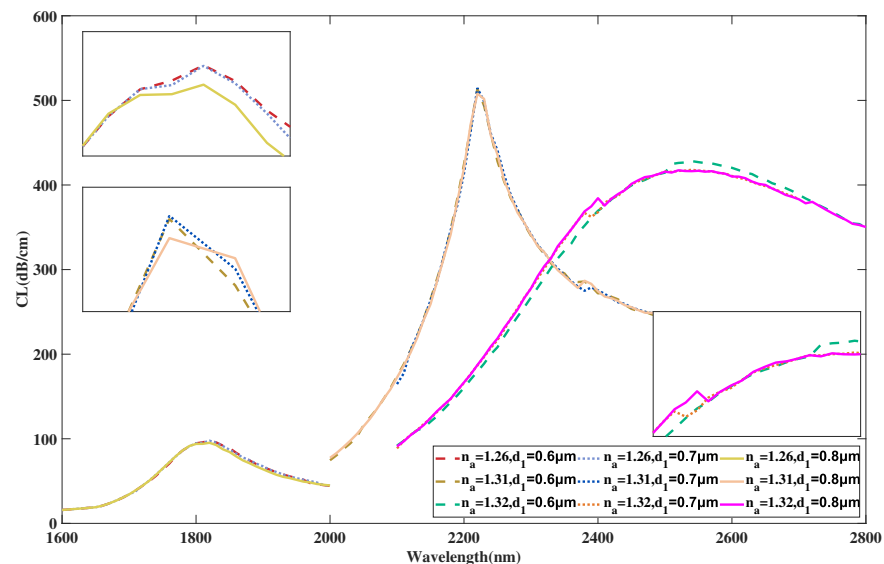


Figure 11. The CL curve of coupled mode in x -polarization when d_1 is selected as 0.6, 0.7, 0.8 μm , and RI is chosen as 1.26, 1.31, 1.32.

Figure 12 demonstrates the CL curve of the coupled mode in x -polarization when L is selected as 5.2, 5.6, 6.0 μm , t is chosen as 50, 60, 70 nm, and there is a variation of RI from 1.26 to 1.34. From Figure 12, with an increasing value of L from 5.2 to 6.0 μm , sensing coverage of RI is gradually narrowed. As seen in Figure 12a,d,g,b,e,h, sensing scope is from 1.26 to 1.33 when L is set as 5.2 μm . When L is set as 5.6 and 6.0 μm , the proposed sensor structure achieves a narrowed sensing scope from 1.26 to 1.32. As seen in Figure 12c,f,i, sensing scope is from 1.26 to 1.34 when L is set as 5.2 μm . When L is set as 5.6 μm , the proposed sensor structure achieves a narrowed sensing coverage from 1.26 to 1.33. When L is set as 6.0 μm , the sensing scope of proposed sensor structure is further narrowed from 1.26 to 1.32. Reasons for these changes are considered that when value of L becomes larger, the amount of coating increases and area A is significantly compressed. Thus the intensity of the envelope demonstrates a trend from increase to decrease. Also, the increasing value of t changes the amount of Au coating too. Moreover, the variation of L influences mode field distribution at the right side of area A in proposed sensor structure, which has an effect on the phase-matching condition of the coupled mode

of area A in x -polarization and causes the CL curve and peak to demonstrate a visible change. According to calculation in Equation (4), the maximum values of S_n are achieved as 18,500, 29,000, 21,000, 22,000, 32,000, 25,000, 26,000, 18,000, 31,000 nm/RIU for scenarios in Figure 12a–i, respectively. Moreover, the average S_n values achieved are 10,642, 10,714, 10,125, 12,500, 12,000, 10,857, 14,600, 12,833, 12,667 nm/RIU for scenarios in Figure 12a–i, respectively. When the maximum S_n value is given priority to be taken into consideration, values of L and t are set as 5.6 μm and 60 nm when the proposed sensor structure achieves an optimal sensing performance.

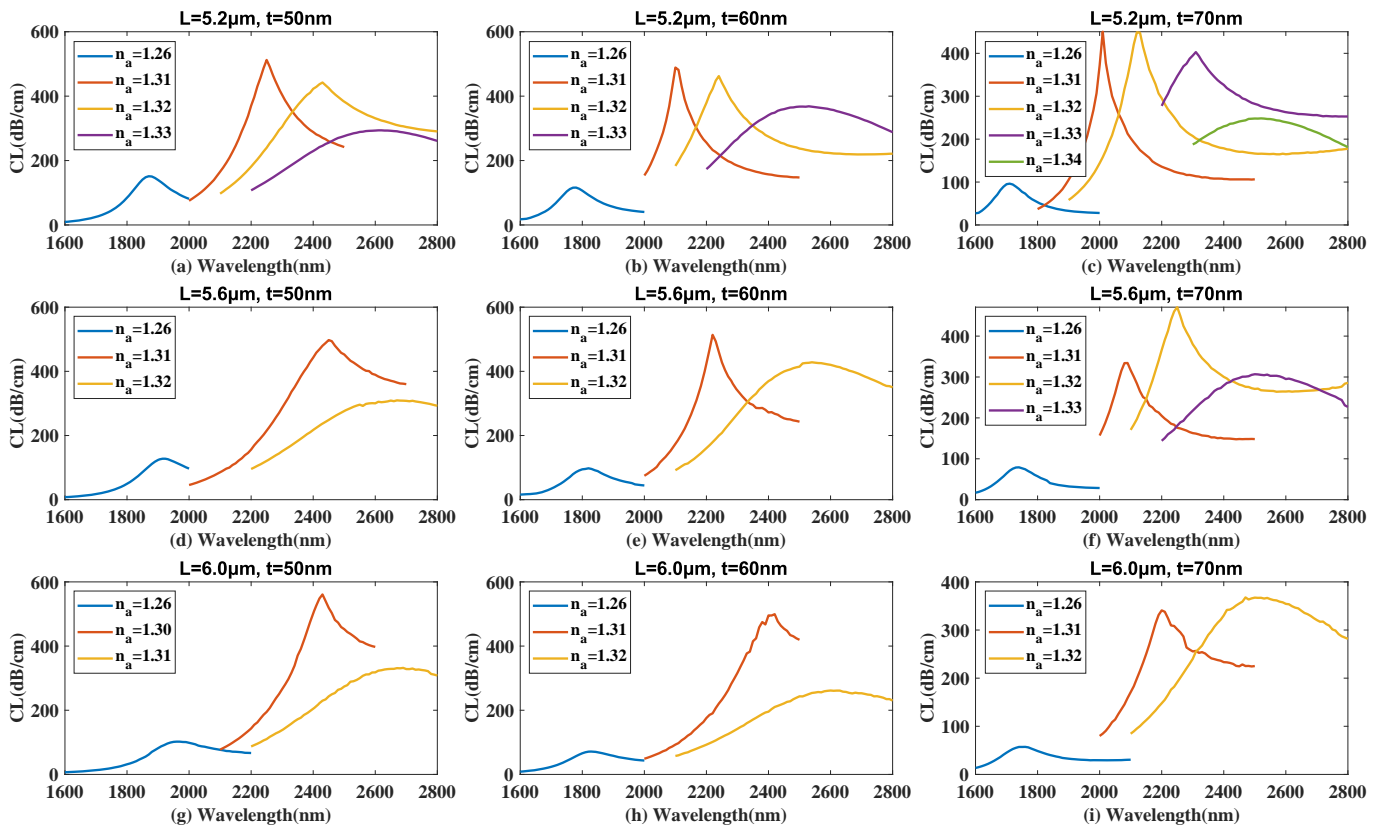


Figure 12. The CL curve of coupled mode in x -polarization when L is selected as 5.2, 5.6, 6.0 μm , t is chosen as 50, 60, 70 nm, and a variation of RI from 1.26 to 1.34.

Figure 13 shows the CL curve of the coupled mode in x -polarization when d_0 is selected as 0.1, 0.2, 0.3 μm , and RI is chosen as 1.26, 1.31, 1.32 and 1.33. From Figure 13, with an increasing value of d_0 from 0.1 to 0.3 μm , the CL curve of the mode with RI selected as 1.26 almost does not shift and the curve intensity demonstrates a dramatic decrease. The CL curve of the mode demonstrates a small red shift and its intensity first increases and then decreases when RI is chosen as the maximum value of RI sensing coverage for all chosen d_0 values. In addition, with d_0 increases, the envelope of the CL curves associated with varying RI demonstrates a visible red shift and becomes narrow along with a decrease in envelope intensity. Additionally, the sensing scope is extended to 1.33 when d_0 increases to 0.3 μm . The reason for these changes is considered to be that when value of d_0 becomes larger, the channel between core area A and the coating surface is narrowed, which influences the mode field distribution. Also, the variation of d_0 changes the area for the SPR effect, which has a visible influence on the phase-matching condition of the coupled mode of x -polarized area A and further causes an obvious change in the CL curve along with the appearance of a new sensing RI 1.33. Moreover, with the channel narrowed, the core area is further isolated, which affects the mode couple. Thus, the intensity of the envelope illustrates a trend from ascending to descending. According to calculation in Equation (4), the maximum S_n values are achieved as 26,200, 32,000, 27,000 nm/RIU when

d_0 is selected as 0.1, 0.2, 0.3 μm , respectively. It is clear from the calculation results that the maximum value of S_n in the proposed design has a trend from rise to decline with a variation of d_0 from 0.1 to 0.3 μm . Moreover, the average value of S_n in the proposed design decreases with a changing sequence of d_0 . In addition, the average S_n values achieved are 12,167, 12,000, 11,143 nm/RIU when d_0 is selected as 0.1, 0.2, 0.3 μm , respectively. When the maximum S_n value and fabrication difficulty are considered priorities, the value of d_0 is finally set as 0.2 μm , resulting in the proposed sensor structure achieving an optimal sensing performance.

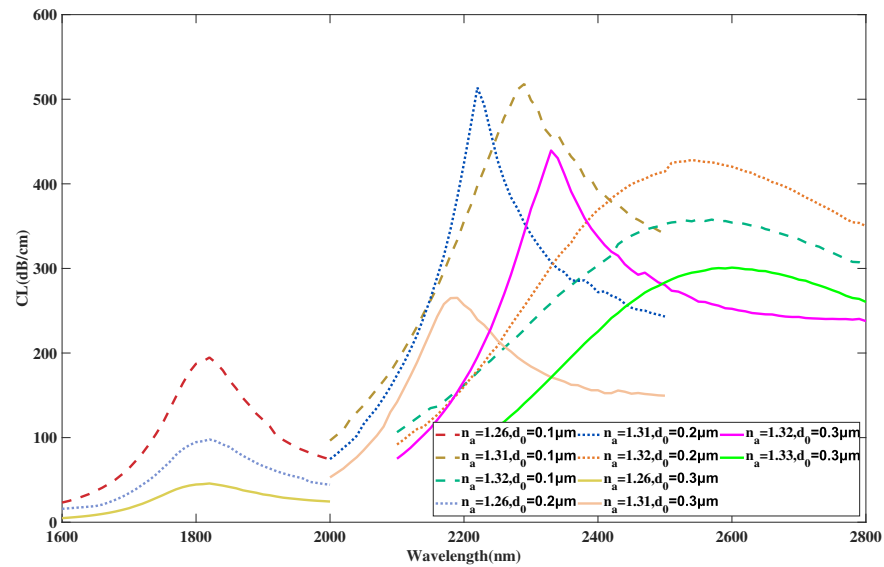


Figure 13. The CL curve of coupled mode in x -polarization when d_0 is selected as 0.1, 0.2, 0.3 μm , and RI is chosen as 1.26, 1.31, 1.32 and 1.33.

Figure 14 illustrates the CL curve of the coupled mode in x -polarization when a is set as 0.7, 0.9, 1.1 μm , b is fixed at 0.4 μm , and RI is chosen as 1.26, 1.31, 1.32. From Figure 14, with an increasing value of a from 0.7 to 1.1 μm when b is fixed at 0.4 μm , the CL curve starts to red-shift and the related curve intensity demonstrates a slight increase when RI is set as 1.26. The CL curve when RI is set as 1.31 has a noticeable red-shift and its intensity first rises and then drops. The CL curve with RI chosen as 1.32 demonstrates a visible red-shift and its intensity demonstrates a dramatic decrease. In addition, with the value of a increasing, the envelope of the CL curves associated with varying RI demonstrates a red shift and appears to become broader. Moreover, the intensity of the envelope shows a trend from climbing to falling when a increases. The reason for these changes are considered to be that when the value of a becomes larger, the core region area A is gradually horizontally compressed, influencing the mode field distribution. This further alters the phase-matching condition of the x -polarized coupled mode of area A and further causes the slight shift of the CL curve and peak. Additionally, the variations in the core area alter the concentration of energy, causing a change in the envelope intensity. According to calculation in Equation (4), the maximum S_n values are achieved as 30,500, 32,000, 30,500 nm/RIU when a is chosen as 0.7, 0.9, 1.1 μm , respectively. It is obvious from the calculation results that the maximum value of S_n in the proposed design shows a trend from increase to decrease with a variation of a from 0.7 to 1.1 μm . Additionally, the calculated average S_n value of the proposed design increases when a changes from 0.7 to 1.1 μm . Moreover, the average S_n values achieved are 11,500, 12,000, 12,667 nm/RIU when a is selected as 0.7, 0.9, 1.1 μm , respectively. Taking both S_n values and fabrication difficulties into account, the value of a is finally set as 0.9 μm when the proposed sensor structure achieves an optimal sensing performance.

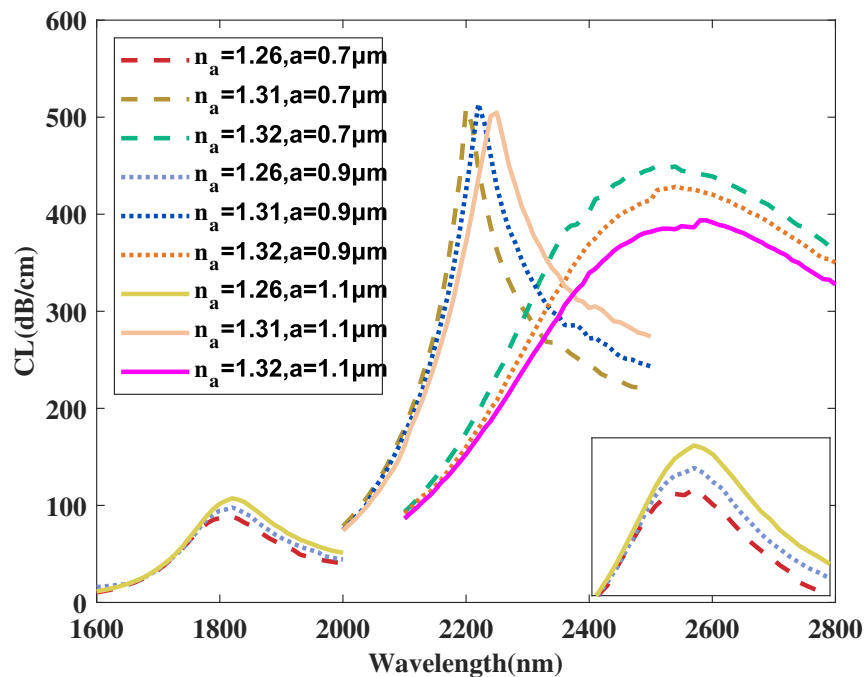


Figure 14. The CL curve of coupled mode in x -polarization when a is set as 0.7, 0.9, 1.1 μm , b is fixed at 0.4 μm , and RI is chosen as 1.26, 1.31, 1.32.

Figure 15 demonstrates the CL curve of the coupled mode in x -polarization when b is set as 0.2, 0.4, 0.6 μm , a is fixed at 0.9 μm , and RI is chosen as 1.26, 1.31, 1.32. From Figure 15, when b increases from 0.2 to 0.6 μm when a is fixed at 0.9 μm , the CL curve starts to red-shift and the related curve intensity demonstrates a slight increase when RI has a variation sequence from 1.26 to 1.31. Also, when RI changes from 1.31 to 1.32, the CL curve of this design has a significant red-shift and the intensity decreases. In addition, with an increasing value of b , the envelope of CL curves associated with varying RI values demonstrates a red shift and becomes broader. The reason for these changes are considered to be that when value of b becomes larger, core region area A is vertically compressed to a certain degree, influencing the mode field distributions. This also alters the phase-matching condition of the x -polarized coupled mode of area A and further causes the slight shift in the CL curve and peak. Meanwhile, the change of the core area in the vertical direction has little influence on the concentration of the energy. Thus, the change of envelope intensity is small. According to calculation in Equation (4), maximum S_n values are achieved as 31,000, 32,000, 31,000 nm/RIU when b is chosen as 0.2, 0.4, 0.6 μm , respectively. It is clear from the calculation results that the maximum value of S_n in the proposed design illustrates a trend from rise to decline with a variation of b from 0.2 to 0.6 μm . Additionally, the calculated average S_n value of the proposed structure increases with b changing from 0.2 to 0.6 μm . Moreover, the average S_n values achieved are 11,333, 12,000, 12,167 nm/RIU when b is chosen as 0.2, 0.4, 0.6 μm , respectively. When maximum S_n value is considered a priority, the value of b is finally chosen as 0.4 μm when the proposed sensor structure achieves an optimal sensing performance.

For the design in this correspondence, a sensitivity analysis of the single structural parameter to sensing performances of the proposed design has been explored and summarized in Table 2, as below.

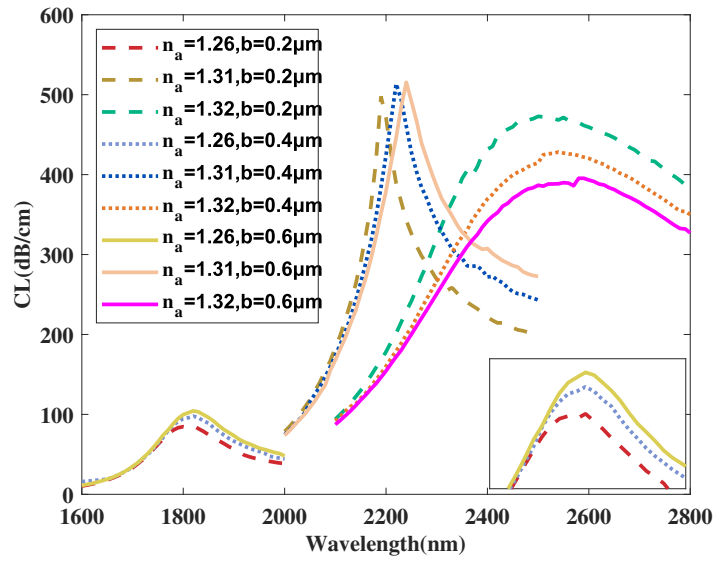


Figure 15. The CL curve of coupled mode in *x*-polarization when *b* is set as 0.2, 0.4, 0.6 μm, *a* is fixed at 0.9 μm, and RI is chosen as 1.26, 1.31, 1.32.

Table 2. Sensitivity analysis of single structural parameter to sensing performances of proposed design.

Parameter	λ_{SPR} ¹	Max S_n Value	Max S_n Value	Envelope	RI Coverage	Optimized Value
Λ ↑ ²	Red-Shift	↑↓ ³	↑	Red-Shift, ↓ ⁴	↑↓	2.8 μm
d_0 ↑	Red-Shift	↑↓	↓	Red-Shift, ↓	↑	0.2 μm
d_1 ↑	Unchanged	↓	↓	Unchanged	Unchanged	0.6 μm
d_2 ↑	Red-Shift	↑↓	↑	Red-Shift, ↓	↓	1.1 μm
d_3 ↑	Unchanged	↑	↓↑ ⁵	Unchanged	Unchanged	1.3 μm
t_{Au} ↑	Blue-shift	↑	↑	Blue-shift	↑	60 nm
l_{Au} ↑	Red-shift	↑↓	↓	Red-shift	↑	5.6 μm
a_1 ↑	Red-shift	↑↓	↑	Red-shift	Unchanged	0.9 μm
b_1 ↑	Red-shift	↑↓	↑	Red-shift	Unchanged	0.4 μm

¹ resonant wavelength. ² increases. ³ firstly increases and then decreases. ⁴ decreases. ⁵ firstly decreases and then increases.

5. Sensing Performance

Through the analysis and optimization of the structural parameters as discussed in Section 4 and summarized in Table 2, the final structure is determined, comprising the following list of optimized structural parameters: $\Lambda = 2.8 \mu\text{m}$, $d_0 = 0.2 \mu\text{m}$, $d_1 = 0.6 \mu\text{m}$, $d_2 = 1.1 \mu\text{m}$, $d_3 = 1.3 \mu\text{m}$, $t_{Au} = 60 \text{ nm}$, $l_{Au} = 5.6 \mu\text{m}$, $a_1 = 0.9 \mu\text{m}$, and $b_1 = 0.4 \mu\text{m}$. In this section, simulations are conducted on the final optimized model to analyze the related sensing performances of the proposed design.

Figure 16 depicts CL curves of coupled modes in *x*-polarization corresponding to changing RI values from 1.26 to 1.32. With an increasing RI value from 1.26 to 1.32, the CL curve of the coupled mode in *x*-polarization starts to significantly red-shift. Additionally, the associated curve intensity exhibits a visible trend of rise to decline as the RI varies from 1.26 to 1.32. λ_{SPR} , representing the wavelength at which the maximum value of the CL curve occurs, signifying complete SPR effect and full coupling, follows the sequence: 1810, 1860, 1920, 2000, 2090, 2220, 2540 nm as the RI changes from 1.26 to 1.32 with increments of 0.01 RIU. According to Equation (4), the corresponding S_n values for different RI intervals

can be calculated as 5000, 6000, 8000, 9000, 13,000, and 32,000 nm/RIU, respectively. Additionally, the average S_n value of the designed sensor is obtained as 12,167 nm/RIU. It can be further concluded that the proposed sensor achieves a maximum resolution of 3.125×10^{-6} RIU within a measurement range from 1.26 to 1.32.

Figure 17 illustrates AS curves of coupled modes in x -polarization corresponding to changing RI values from 1.26 to 1.31. With an increasing RI value from 1.26 to 1.31, AS curves of coupled modes in x -polarization experience a significant red-shift. λ_{peak} , representing the wavelength at which the maximum absolute value of the negative semi-axis in the AS curve occurs, follows the sequence: 1910, 1970, 2030, 2110, 2220, 2540 nm with RI varying as 1.26, 1.27, 1.28, 1.29, 1.30, 1.31. From Figure 17 and Equation (5), the maximum absolute value of S_a for all curves is obtained as 67.35, 75.83, 90.36, 116.5, 176, and 85.92 RIU⁻¹, respectively.

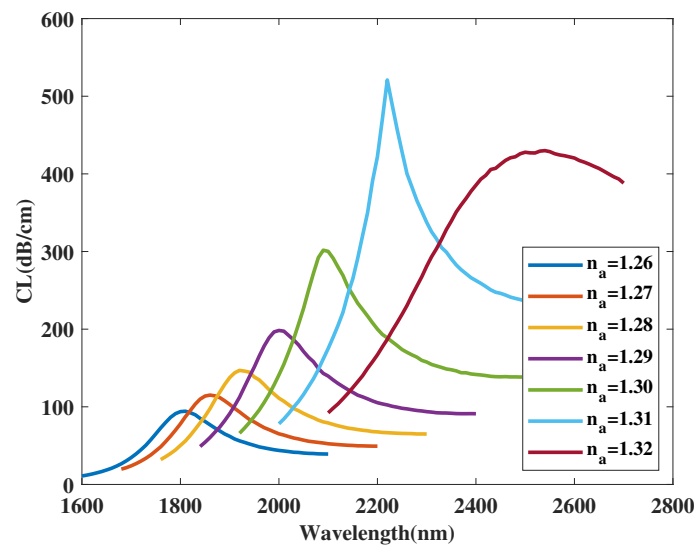


Figure 16. CL curves of coupled mode in x -polarization corresponded to a changing value of RI from 1.26 to 1.32.

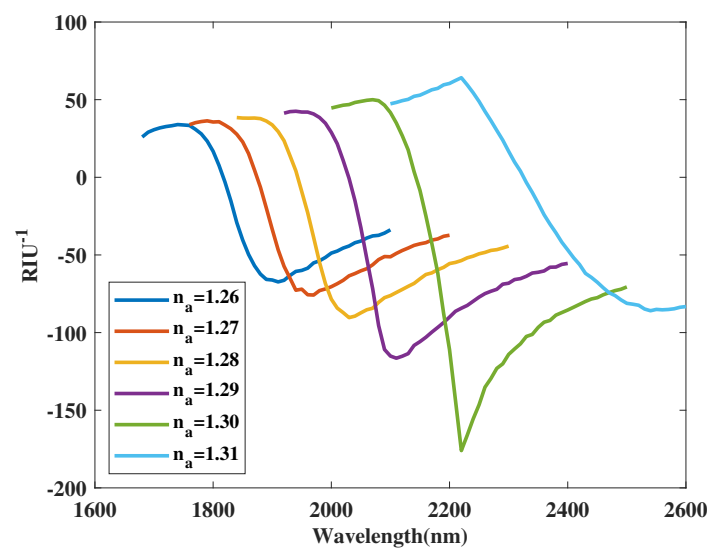


Figure 17. AS curves of coupled mode in x -polarization corresponded to a changing value of RI from 1.26 to 1.31.

Moreover, metrics such as FOM can be calculated according to Equation (6). All sensing performances of this design are summarized and listed in Table 3.

Table 3. Sensing performance summary of designed sensor in this work.

RI	λ_{SPR} (nm)	$\Delta\lambda_{SPR}$ (nm)	FWHM (nm)	S_n (nm/RIU)	FOM (RIU ⁻¹)	λ_{peak} (nm)	$ S_a $ (RIU ⁻¹)
1.26	1810	50	235	5000	21.3	1910	67.35
1.27	1860	60	255	6000	23.5	1970	75.83
1.28	1920	80	295	8000	27.1	2030	90.36
1.29	2000	90	335	9000	26.9	2110	116.5
1.30	2090	130	320	13,000	40.6	2220	176
1.31	2220	320	250	32,000	128.0	2540	85.92
1.32	2540	N/A	N/A	N/A	N/A	N/A	N/A

It is important to note that the measurement range of this sensor is constrained within a specific scope. Measurements conducted beyond this range may not produce reliable results. As seen in Figure 16, as the RI value varies from 1.26 to 1.32, the red shift of the CL curve becomes more pronounced. When the RI is below 1.26, it's evident that the degree of red shift is negligible. This would significantly reduce the average sensitivity value, thereby affecting the performance of the proposed structure. Furthermore, the intensity of the loss curve is close to zero when the RI is below 1.26, which also impacts the performance of the AS curve. On the other hand, when the RI value exceeds 1.32, the SPR effect becomes obstructed, leading to divergent results in the simulated CL curve. In such cases, the outcomes become invalid for measurement purposes. Increasing the lower boundary value of the sensing scope can elevate the average sensitivity value for these minor-shifted loss curves when the RI is low, consequently enhancing the design's performance to some extent. However, this adjustment simultaneously narrows down the measurement coverage of the design. After considering both the advantages and disadvantages, the RI measurement range is ultimately chosen to be between 1.26 and 1.32.

Table 4 is the baseline of sensing performances in proposed design compared with related works. In other designs, a variety of geometrical constructions are proposed to form areas for the couple of basic core-guided modes and different-order SPP modes with different kinds of polarization states to excite SPR effect in order to achieve measurement of physical values in systems. In this correspondence, the designed polished-D-shape fiber sensor achieves measurement of RI with wavelength range from 1810 to 2540 nm and a sensing RI coverage from 1.26 to 1.32. Also, the realize of modes coupling is significant distinct in dB/cm-scale intensity between x - and y -polarization, which further forms a well single-polarization sensing performance.

Table 4. Baseline of sensing performances in proposed design compared with related works.

λ (nm) Coverage	RI Coverage	Maximum S_n (nm/RIU)	Average S_n (nm/RIU)	Refs.
670~1120	1.33~1.38	25,000	9000	[39]
1548~2683	1.423~1.523	12,500	11,350	[40]
550~780	1.368~1.401	4078.43	N/A	[41]
600~900	1.35~1.41	6214.28	N/A	[42]
560~993	1.33~1.41	13,750	6185.7	[43]
1810~2540	1.26~1.32	32,000	12,167	This work

6. Conclusions

In conclusion, an innovative SPR-PCF sensor structure in the form of a polished-D-shape has been designed and optimized for the purpose of measuring analyte refractive index (RI). This design involves the assembly of various capillaries, which are further processed to create a polished-D-shaped structure. The flattened surface of this structure is coated with nano-scale gold material. By incorporating a nano-scale thin gold coating and a solid silica-background core region (area A), the SPR effect is excited and enhanced. Consequently, the CL curve experiences a noticeable red shift as the RI increases. The

proposed sensor structure covers a resonant wavelength range spanning from 1810 to 2540 nm, catering to the measurement scenario. Through simulation and calculation, the designed sensor achieves maximum and average S_n values of 32,000 and 12,167 nm/RIU, respectively, within an RI range of 1.26 to 1.32. These remarkable sensing performance characteristics render the proposed structure advantageous for the detection of organic biomedicine and other related applications.

Author Contributions: Conceptualization, W.L. and H.Z.; methodology, H.Z.; software, W.L.; validation, M.J.; formal analysis, W.L. and J.X.; investigation, Y.C.; resources, W.L. and M.J.; data curation, W.L. and J.X.; writing—original draft preparation, W.L.; writing—review and editing, W.L. and H.Z.; visualization, W.L. and Y.C.; supervision, H.Z.; project administration, H.Z. All authors have read and agreed to the published version of the manuscript.

Funding: This research received no external funding.

Data Availability Statement: The datasets corresponding to this article can be provided to readers with a reasonable request.

Conflicts of Interest: All authors declare no conflict of interest.

Abbreviations

Abbreviations applied in this article are shown as follows:

AS	Amplitude Sensitivity
CL	Confinement Loss
FEM	Finite Element Method
FOM	Figure of Merit
Hi-Bi	High-Birefringence
OSA	Optical Spectrum Analyzer
PCF	Photonic Crystal Fiber
RI	Refractive Index
SMF	Single Mode Fiber
SPP	Surface Plasmon Polariton
SPR	Surface Plasmon Resonance
WS	Wavelength Sensitivity

References

1. Li, H.; Zhang, L. Photocatalytic performance of different exposed crystal facets of BiOCl. *Curr. Opin. Green Sustain. Chem.* **2017**, *6*, 48–56. [[CrossRef](#)]
2. Zhu, X.; Gao, T. Chapter 10—Spectrometry. In *Nano-Inspired Biosensors for Protein Assay with Clinical Applications*; Li, G., Ed.; Elsevier: Amsterdam, The Netherlands, 2019; pp. 237–264. [[CrossRef](#)]
3. Homola, J.; Koudela, I.; Yee, S.S. Surface plasmon resonance sensors based on diffraction gratings and prism couplers: Sensitivity comparison. *Sens. Actuators B Chem.* **1999**, *54*, 16–24. [[CrossRef](#)]
4. Dahan, R.; Nehemia, S.; Shentcis, M.; Reinhardt, O.; Adiv, Y.; Shi, X.; Be'er, O.; Lynch, M.H.; Kurman, Y.; Wang, K.; et al. Resonant phase-matching between a light wave and a free-electron wavefunction. *Nat. Phys.* **2020**, *16*, 1123–1131. [[CrossRef](#)]
5. Yesudasu, V.; Pradhan, H.S.; Pandya, R.J. Recent progress in surface plasmon resonance based sensors: A comprehensive review. *Heliyon* **2021**, *7*, e06321. [[CrossRef](#)] [[PubMed](#)]
6. Shafkat, A.; Rashed, A.; el hageen, H.; Alatwi, A. Design and analysis of a single elliptical channel photonic crystal fiber sensor for potential malaria detection. *J. Sol-Gel Sci. Technol.* **2021**, *98*, 202–211. [[CrossRef](#)]
7. Huang, L.; Tian, H.; Zhou, J.; Ji, Y. Design Low Crosstalk Ring-Slot Array Structure for Label-Free Multiplexed Sensing. *Sensors* **2014**, *14*, 15658–15668. [[CrossRef](#)]
8. O'Brien, J.; Pryde, G.; White, A.; Ralph, T.; Branning, D. Demonstration of an all-optical quantum controlled-NOT gate. *Nature* **2003**, *426*, 264–267. [[CrossRef](#)]
9. Wu, Y.D.; Shih, T.T.; Lee, J.J. High-quality-factor filter based on a photonic crystal ring resonator for wavelength division multiplexing applications. *Appl. Opt.* **2009**, *48*, F24–F30. [[CrossRef](#)]
10. Hosseini, A.; Xu, X.; Subbaraman, H.; Lin, C.Y.; Rahimi, S.; Chen, R.T. Large optical spectral range dispersion engineered silicon-based photonic crystal waveguide modulator. *Opt. Express* **2012**, *20*, 12318–12325. [[CrossRef](#)] [[PubMed](#)]
11. Parandin, F.; Heidari, F.; Aslinezhad, M.; Parandin, M.; Roshani, S.; Roshani, S. Design of 2D photonic crystal biosensor to detect blood components. *Opt. Quantum Electron.* **2022**, *54*, 618. [[CrossRef](#)]

12. Markos, C.; Travers, J.C.; Abdolvand, A.; Eggleton, B.J.; Bang, O. Hybrid photonic-crystal fiber. *Rev. Mod. Phys.* **2017**, *89*, 045003. [[CrossRef](#)]
13. Prabowo, B.A.; Purwidyantri, A.; Liu, K.C. Surface Plasmon Resonance Optical Sensor: A Review on Light Source Technology. *Biosensors* **2018**, *8*, 80. [[CrossRef](#)] [[PubMed](#)]
14. Liu, C.; Lü, J.; Liu, W.; Wang, F.; Chu, P. Overview of refractive index sensors comprising photonic crystal fibers based on the surface plasmon resonance effect. *Chin. Opt. Lett.* **2021**, *19*, 102202. [[CrossRef](#)]
15. Ramya, K.C.; Monfared, Y.E.; Maheswar, R.; Dhasarathan, V. Dual-Core Twisted Photonic Crystal Fiber Salinity Sensor: A Numerical Investigation. *IEEE Photonics Technol. Lett.* **2020**, *32*, 616–619. [[CrossRef](#)]
16. Mollah, M.A.; Islam, S.R.; Yousufali, M.; Abdulrazak, L.F.; Hossain, M.B.; Amiri, I. Plasmonic temperature sensor using D-shaped photonic crystal fiber. *Results Phys.* **2020**, *16*, 102966. [[CrossRef](#)]
17. Huang, H.; Zhang, Z.; Yu, Y.; Zhou, L.; Tao, Y.; Li, G.; Yang, J. A Highly Magnetic Field Sensitive Photonic Crystal Fiber Based on Surface Plasmon Resonance. *Sensors* **2020**, *20*, 5193. [[CrossRef](#)]
18. Chen, X.; Xia, L.; Li, C. Surface Plasmon Resonance Sensor Based on a Novel D-Shaped Photonic Crystal Fiber for Low Refractive Index Detection. *IEEE Photonics J.* **2018**, *10*, 1–9. [[CrossRef](#)]
19. Chao, C.T.C.; Chen, S.H.; Huang, H.J.; Kooh, M.R.R.; Lim, C.M.; Thotagamuge, R.; Mahadi, A.H.; Chau, Y.F.C. Improving Temperature-Sensing Performance of Photonic Crystal Fiber via External Metal-Coated Trapezoidal-Shaped Surface. *Crystals* **2023**, *13*, 813. [[CrossRef](#)]
20. Bing, P.; Sui, J.; Wu, G.; Guo, X.; Li, Z.; Tan, L.; Yao, J. Analysis of Dual-Channel Simultaneous Detection of Photonic Crystal Fiber Sensors. *Plasmonics* **2020**, *15*, 1071–1076. [[CrossRef](#)]
21. Han, B.; nan Zhang, Y.; E, S.; Wang, X.; Yang, D.; Wang, T.; Lu, K.; Wang, F. Simultaneous measurement of temperature and strain based on dual SPR effect in PCF. *Opt. Laser Technol.* **2019**, *113*, 46–51. [[CrossRef](#)]
22. Subramanian, S.; Wu, H.Y.; Constant, T.; Xavier, J.; Vollmer, F. Label-Free Optical Single-Molecule Micro- and Nanosensors. *Adv. Mater.* **2018**, *30*, 1801246. [[CrossRef](#)] [[PubMed](#)]
23. Soler, M.; Lechuga, L. Biochemistry strategies for label-free optical sensor biofunctionalization: Advances towards real applicability. *Anal. Bioanal. Chem.* **2021**, *414*. [[CrossRef](#)] [[PubMed](#)]
24. Chao, C.T.C.; Kooh, M.R.R.; Chau, Y.F.C.; Thotagamuge, R. Susceptible Plasmonic Photonic Crystal Fiber Sensor with Elliptical Air Holes and External-Flat Gold-Coated Surface. *Photonics* **2022**, *9*, 916. [[CrossRef](#)]
25. Azman, M.F.; Mahdiraji, G.A.; Wong, W.R.; Aoni, R.A.; Adikan, F.R.M. Design and fabrication of copper-filled photonic crystal fiber based polarization filters. *Appl. Opt.* **2019**, *58*, 2068–2075. [[CrossRef](#)]
26. Malitson, I.H. Interspecimen Comparison of the Refractive Index of Fused Silica. *J. Opt. Soc. Am.* **1965**, *55*, 1205–1209. [[CrossRef](#)]
27. Tan, C. Determination of refractive index of silica glass for infrared wavelengths by IR spectroscopy. *J. Non-Cryst. Solids* **1998**, *223*, 158–163. [[CrossRef](#)]
28. Vial, A.; Grimault, A.S.; Macías, D.; Barchiesi, D.; de la Chapelle, M.L. Improved analytical fit of gold dispersion: Application to the modeling of extinction spectra with a finite-difference time-domain method. *Phys. Rev. B* **2005**, *71*, 085416. [[CrossRef](#)]
29. Liu, Q.; Li, S.; Chen, H.; Li, J.; Fan, Z. High-sensitivity plasmonic temperature sensor based on photonic crystal fiber coated with nanoscale gold film. *Appl. Phys. Express* **2015**, *8*, 046701. [[CrossRef](#)]
30. Chau, Y.F.; Yeh, H.H.; Tsai, D.P. Significantly Enhanced Birefringence of Photonic Crystal Fiber Using Rotational Binary Unit Cell in Fiber Cladding. *Jpn. J. Appl. Phys.* **2007**, *46*, L1048. [[CrossRef](#)]
31. Lopez, G.; Estevez, M.C.; Soler, M.; Lechuga, L. Recent advances in nanoplasmonic biosensors: Applications and lab-on-a-chip integration. *Nanophotonics* **2016**, *6*, 123–136. [[CrossRef](#)]
32. Ekgasit, S.; Thammacharoen, C.; Yu, F. Evanescent Field in Surface Plasmon Resonance and Surface Plasmon Field-Enhanced Fluorescence Spectroscopies. *Anal. Chem.* **2004**, *76*, 2210–2219. [[CrossRef](#)]
33. Yan, X.; Wang, Y.; Cheng, T.; Li, S. Photonic Crystal Fiber SPR Liquid Sensor Based on Elliptical Detective Channel. *Micromachines* **2021**, *12*, 408. [[CrossRef](#)]
34. Mittal, S.; Sharma, T.; Tiwari, M. Surface plasmon resonance based photonic crystal fiber biosensors: A review. *Mater. Today Proc.* **2021**, *43*, 3071–3074. [[CrossRef](#)]
35. Mitu, S.; Ahmed, K.; Hossain, M.; Paul, B.K.; Nguyen, T.; D, V. Design of Magnetic Fluid Sensor Using Elliptically Hole Assisted Photonic Crystal Fiber (PCF). *J. Supercond. Nov. Magn.* **2020**, *33*, 2189–2198. [[CrossRef](#)]
36. Rifat, A.A.; Ahmed, R.; Yetisen, A.K.; Butt, H.; Sabouri, A.; Mahdiraji, G.A.; Yun, S.H.; Adikan, F.M. Photonic crystal fiber based plasmonic sensors. *Sens. Actuators B Chem.* **2017**, *243*, 311–325. [[CrossRef](#)]
37. Rahad, R.; Rakib, A.; Mahadi, M.K.; Faruque, M.O. Fuel classification and adulteration detection using a highly sensitive plasmonic sensor. *Sens. Bio-Sens. Res.* **2023**, *40*, 100560. [[CrossRef](#)]
38. Sorathiya, V.; Lavadiya, S.; Faragallah, O.; Eid, M.; Rashed, A. 3 D shaped dual core photonics crystal based refractive index sensor using graphene-titanium-silver materials for infrared frequency spectrum. *Opt. Quantum Electron.* **2022**, *54*, 290. [[CrossRef](#)]
39. Islam, M.; Cordeiro, C.; Sultana, J.; Aoni, R.A.; Feng, S.; Ahmed, R.; Dorraki, M.; Dinovitser, A.; Ng, B.; Abbott, D. A Hi-Bi Ultra-Sensitive Surface Plasmon Resonance Fiber Sensor. *IEEE Access* **2019**, *7*, 79085–79094. [[CrossRef](#)]
40. Liao, J.; Ding, Z.; Xie, Y.; Wang, X.; Zeng, Z.; Huang, T. Ultra-broadband and highly sensitive surface plasmon resonance sensor based on four-core photonic crystal fibers. *Opt. Fiber Technol.* **2020**, *60*, 102316. [[CrossRef](#)]

41. Ibrahim, K.; Kumar, R.; Pakhira, W. Enhance the Design and Performance Analysis of a Highly Sensitive Twin-Core PCF SPR Biosensor with Gold Plating for the Early Detection of Cancer Cells. *Plasmonics* **2023**, *18*, 995–1006. [[CrossRef](#)]
42. Abdelghaffar, M.; Gamal, Y.; El-Khoribi, R.; Soliman, W.; Badr, Y.; Hameed, M.; Obayya, S. Highly sensitive V-shaped SPR PCF biosensor for cancer detection. *Opt. Quantum Electron.* **2023**, *55*, 472. [[CrossRef](#)]
43. Li, K.; Guo, Y.; Li, S.G.; Yin, Z.; Chen, Q.; Meng, X.; Gao, Z.; Bai, G. High Sensitivity Refractive Index Sensor Based on D-Shaped Photonic Crystal Fiber Coated with Graphene-Silver Films. *Plasmonics* **2023**, *18*, 1093–1101. [[CrossRef](#)]

Disclaimer/Publisher's Note: The statements, opinions and data contained in all publications are solely those of the individual author(s) and contributor(s) and not of MDPI and/or the editor(s). MDPI and/or the editor(s) disclaim responsibility for any injury to people or property resulting from any ideas, methods, instructions or products referred to in the content.